

Free-energy landscape of a polymer in the presence of two nanofluidic entropic traps

James M. Polson¹ and Matthew Kozma¹

Department of Physics, University of Prince Edward Island, 550 University Avenue, Charlottetown, Prince Edward Island, C1A 4P3, Canada

(Dated: 9 September 2024)

Recently, nanofluidics experiments have been used to characterize the behavior of single DNA molecules confined to narrow slits etched with arrays of nanopits. Analysis of the experimental data relies on analytical estimates of the underlying free-energy landscape. In this study we use computer simulations to explicitly calculate the free energy and test the approximations employed in such analytical models. Specifically, Monte Carlo simulations were used to study a polymer confined to complex geometry consisting of a nanoslit with two square nanopits embedded in one of the surfaces. The two-dimensional Weighted Histogram Analysis Method (WHAM2D) is used to calculate the free energy, F , as a function of the sum (λ_1) and the difference (λ_2) of the length of the polymer contour contained in the two nanopits. We find the variation of the free-energy function with respect to confinement dimensions to be comparable to the analytical predictions that employ a simplistic theoretical model. However, there are some noteworthy quantitative discrepancies, particularly between the predicted and observed variation of F with respect to λ_1 . Our study provides a useful lesson on the limitations of using simplistic analytical expressions for polymer free-energy landscapes to interpret results for experiments of DNA confined to a complex geometry and points to the value of carrying out accurate numerical calculations of the free energy instead.

I. INTRODUCTION

Confinement of a polymer chain to a space with dimensions smaller than its radius of gyration strongly affects its conformational and dynamical properties. Of particular note is the case of simple confinement geometries such as a slit or a long channel, where a single length scale (i.e., slit height, channel width) characterizes the degree of confinement. Over the past two decades, such systems have been extensively examined experimentally using fluorescence microscopy of labeled DNA molecules. As a consequence of this work, as well as that of studies of confined polymers using simulation and theoretical methods, the behaviour of these basic systems is now well understood.^{1–13}

In addition to simple confinement geometries, there has also been increasing interest in characterizing the behaviour of polymers confined to more complex spaces featuring locally varying dimensionality and confinement scale. Examples include confinement of DNA in 2D arrays of spherical cavities connected by narrow pores,¹⁴ as well as DNA stretched in a nanoslit between two microcavities or reservoirs.^{15–19} Another example is a dual-nanopore device employing DNA “flossing” to exchange contour between two microcavities, recently used to estimate the contour distance between physical tags installed at sequence motifs^{20,21} to provide electronic mapping of bacterial genome.²²

Another collection of studies have carried out nanofluidics experiments to examine the configurational and dynamical behaviour of DNA confined to complex geometries composed of a nanoslit with parallel arrays of nanogrooves^{23–25} and nanopits^{26–31} etched into one surface of the slit. The pits and grooves act as entropic traps and generate a free-energy landscape that governs

the equilibrium dynamics of the polymer. In the case of the nanopit geometry, manipulation of the confinement dimensions (i.e., slit height and nanopit width, depth and separation) can create conditions wherein the polymer prefers to span two or more pits. From such a tuning of the free-energy landscape has emerged novel phenomena such as diffusion resonance²⁷ as well as collective wave-like excitations for excess concentration of DNA that span many nanocavities.³⁰ In addition, the dynamical behaviour of DNA in such systems has been shown to provide a means to measure its effective width.²⁹

Central to the analysis of the data from many DNA experiments employing such nanotopographies is an analytical estimate of the underlying free-energy landscape. A typical approach is to construct composite theoretical models using established results for confinement in simple geometries. For example, a polymer with its contour spanning two or more nanopits embedded in a slit surface can be divided into different sections, one for each of the portions occupying the cavities and one for each connecting strand lying in the slit between the cavities. Standard expressions for confinement free energy in cavities and slits can then be used to estimate the contribution from these sections. A noteworthy example is the two-nanopit system of Ref. 28. This study examined the equilibrium dynamics by monitoring the fluctuations in the sum and the difference in the contour length of DNA trapped each of the two nanopits. The fluctuations of these two quantities are governed by the two-dimensional free-energy function near its minimum. The analytical estimate of the free-energy function was used to explain the observed variation in the correlation times for the two modes with respect to confinement dimensions.

Analytical estimates for multi-dimensional free-energy functions for polymers confined to complex geometries

such as that used in Ref. 28 are constructed using simplifying assumptions that may affect their accuracy and thus their utility in the analysis of experimental data. For this reason, it would be helpful to compare these analytical estimates with explicitly calculated free energies. In the present study, we employ Monte Carlo (MC) simulations to calculate such free-energy functions for a simple model polymer confined to a two-nanopit geometry. An illustration of the model system is shown in Fig. 1. Lengthscale ratios for the polymer and confinement dimensions are comparable to those employed in the experiments. As in Ref. 28 we calculate the variation of F with respect to the sum and the difference in the contour length in each of the two pits. The two-dimensional free-energy function is obtained using the 2D Weighted Histogram Analysis Method (WHAM2D).³² We find that the variation of the functions with system dimensions is comparable to the trends observed in the experiments, though we do observe quantitative discrepancies that originate from the breakdown in approximations employed in the theoretical model.

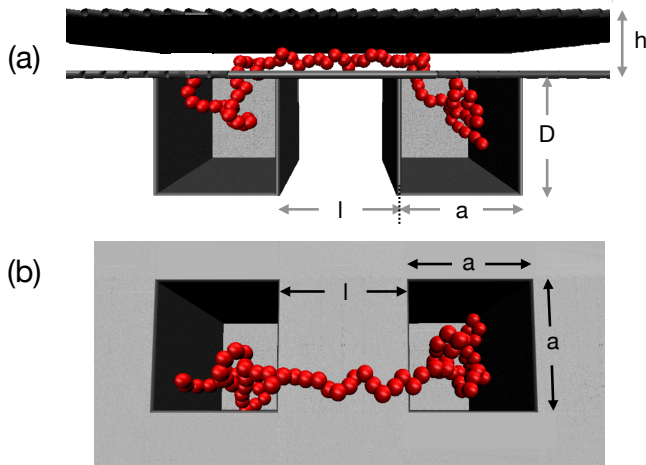


FIG. 1. Illustration of the model system employed in the study. (a) Side view, showing the polymer spanning the two pits embedded in one of the two surfaces of the slit. (b) Top view, with upper surface omitted, for clarity.

The remainder of the paper is organized as follows. Section II describes in detail the model system employed in the study. Next, Sec. III gives an outline of the methodology used together with the relevant details of the simulations. In Section IV we review that analytical model employed in Ref. 28 and tested in this work. Section V presents and discusses the simulation results. Finally, Sec. VI summarizes the main conclusions of this work.

II. MODEL

The system is comprised of a single polymer chain confined to a slit bounded by two infinite parallel planar surfaces separated by a distance h . Embedded in one of the surfaces are two identical pits. The pits each have a square cross section in the lateral directions with a side length of a . In addition, they have a constant depth of D , as measured in the longitudinal direction from the surface into which they are embedded. The nearest edges of the pits are parallel to each other and are separated by a distance l . The various dimensions associated with the confining geometry are illustrated in Fig. 1.

The linear polymer is modeled as a semiflexible chain of N hard spheres of diameter w , which is thus the width of the polymer chain. The bending rigidity of the polymer is modeled using a bending potential with the form, $u_{\text{bend}}(\theta) = \kappa(1 - \cos\theta)$. The angle θ is defined for a consecutive triplet of monomers centered at monomer i such that $\cos\theta_i = \hat{u}_i \cdot \hat{u}_{i+1}$, where \hat{u}_i is the unit vector pointing from monomer $i-1$ to monomer i . The bending constant κ determines the overall stiffness of the polymer and is related to the persistence length P by³³ $\exp(-\langle l_{\text{bond}} \rangle / P) = \coth(\kappa/k_B T) - k_B T / \kappa$, where $\langle l_{\text{bond}} \rangle$ is the mean bond length. For our model, the bond length is fixed to $l_{\text{bond}} = w$. Note that for sufficiently large $\kappa/k_B T \gg 1$ this implies $P/w \approx \kappa/k_B T$. In addition to the polymer bending energy, there are two additional contributions to the total energy that are both athermal in character: the interactions between non-bonded monomers and the monomer-wall interaction. In each case, the energy is infinite in the case of overlap and zero otherwise. System configurations with infinite energy, of course, have zero probability and so are forbidden.

Simulation employed polymer chains of length $N = 1600$ monomers. Typically, the bending rigidity was fixed to $\kappa = 5k_B T$, though in some calculations this value was varied. In addition, most calculations employed confining geometry parameter values of $h = 10w$, $D = 10w$, $a = 60w$, and $l = 60w$. To map the model system onto the experimental system by choosing an effective DNA width of $w = 10$ nm, this corresponds to a contour length of $L = 16 \mu\text{m}$ and a persistence length of $P = 50$ nm, as well as confining geometry parameter values of $h = 100$ nm, $D = 100$ nm, (i.e., $d = h + D = 200$ nm), $a = 600$ nm, and $l = 600$ nm. These values are comparable to the values used in the experiments of Refs. 28 and 29. Simulations were carried out in which each of these parameters were independently varied with the others each fixed to these “standard” values.

III. METHODS

Computer simulations were used to calculate a collection of two-dimensional free-energy functions. In particular, the configurational free energy F is measured as a function of the two quantities $\lambda_1 \equiv N_1 + N_2$ and

$\lambda_2 \equiv N_1 - N_2$, where N_1 and N_2 are the numbers of spherical monomers whose centers lie inside the pits, arbitrarily labeled “1” and “2”. A monomer center is defined to lie inside the pit if it lies within the square cross section of the pit in the lateral plane, independent of its position in the vertical direction. All simulations are carried out using the standard Metropolis Monte Carlo method.^{34,35} We employ a combination of crankshaft and reptation trial moves. In each case, trial moves are rejected if a proposed monomer position overlaps with a surface of the confining geometry. In the absence of such overlap crankshaft moves are accepted with a probability given by the usual Metropolis criterion, where the energy difference between old and new configurations is determined solely from the internal bending energy of the chain. In each simulation the system was equilibrated for a period of 5×10^6 MC cycles, following which quantities were sampled during a production run of 1.1×10^8 MC cycles. One MC cycle corresponds to N attempted crankshaft moves and 10 attempted reptation moves.

In order to improve computational efficiency, we employ the method of cell lists. Since the system is unbounded in the x - y direction, we employ periodic boundaries in these two dimensions using a square simulation box of side length $240w$. Extensive testing showed that this box size was sufficiently large to minimize artificial self-interaction through the periodic boundaries. The cell list method improved the computational efficiency by roughly a factor of two.

In order to calculate the free-energy function, we also use the 2D Weighted Histogram Analysis Method (WHAM2D).³² The procedure requires that a set of individual simulations be carried out, each subject to a unique biasing potential. In each simulation, histories of the values of λ_1 and λ_2 are calculated, and the WHAM2D method constructs an unbiased probability distribution using these histories as input. The method is useful for overcoming problems of poor statistics, particularly in low probability regions. Each calculation employs a quadratic biasing potential of the form

$$U_b = \frac{1}{2}k_1(\lambda_1 - \lambda_1^{(c)})^2 + \frac{1}{2}k_2(\lambda_2 - \lambda_2^{(c)})^2. \quad (1)$$

The coefficients of the potential were chosen to be $k_1 = k_2 = 0.005k_B T/w^2$. In addition, the biasing potential centers were chosen to be spaced by $\Delta\lambda_1^{(c)} = 10w$ over the interval $\lambda_1 \in (0, N)$ and $\Delta\lambda_2^{(c)} = 20w$ over a range of $\lambda_2 \in [-\lambda_1, \lambda_1]$. The latter range follows from the obvious restriction that no pit can contain a greater number of monomers than the total number in both pits. These values of the biasing potential parameters ensure that there is sufficient overlap in the probability distributions between neighboring “potential centers”, as determined by the locations of $\lambda_1^{(c)}$ and $\lambda_2^{(c)}$. Further details about the implementation of the WHAM2D method are presented in Appendix A. In most cases, a calculation to produce a single 2D free energy function required 6801 potential centers, and thus the same number of simula-

tions. As each simulation required approximately 50–60 CPU-hours, each free energy function required up to 47 CPU-years.

In the results presented below, distances are measured in units of w and energy is measured in units of $k_B T$.

IV. THEORY

In this section we employ simple theoretical arguments to predict the functional form of $F(\lambda_1, \lambda_2)$ following the approach in Refs. 28 and 29.

Consider an ideal Gaussian chain of N_K Kuhn segments of length b confined to a rectangular box with dimensions L_x , L_y and L_z . As noted in Ref. 36, the conformational contribution to the configurational partition function is given by:

$$\frac{F_{\text{id,box}}}{k_B T} = \frac{\pi^2 N_K b^2}{6} \left(\frac{1}{L_x^2} + \frac{1}{L_y^2} + \frac{1}{L_z^2} \right). \quad (2)$$

Thus, the confinement free energy of the polymer confined to a box of dimensions $L_x = L_y = a$ and $L_z = d$ is given by

$$\frac{F_{\text{id,box}}}{k_B T} = A_{\text{box}} L, \quad (3)$$

where

$$A_{\text{box}} = \frac{\pi^2 P}{3} \left(\frac{1}{d^2} + \frac{2}{a^2} \right), \quad (4)$$

and where $L = N_K b$ is the contour length and $P = b/2$ is the persistence length. Although derived for a Gaussian chain, this expression is expected to be valid for wormlike chains in the limit where the confinement dimensions are large, i.e. $P \ll d$ and $P \ll a$. In the case where this condition is only marginally satisfied, a numerical calculation is required for a more accurate measure of the free energy. In Ref. 29, Klotz *et al.* performed such a calculation for a wormlike chain confined a pillbox cavity (see Fig. 2(b) of that article). For a real chain, excluded-volume interactions can be incorporated at the second-virial level, $F_{\text{EV}}/k_B T = BL^2$, where

$$B(d, a, w) \equiv \frac{\pi}{4} \frac{w}{V_c}, \quad (5)$$

and where $V_c = da^2$ is the volume of the rectangular cavity. The sum of the two terms, $F_{\text{box}} \equiv F_{\text{id,box}} + F_{\text{EV}}$ is an approximation for the difference in the conformational free energy of a confined real chain and an unconfined ideal chain. This can be written:

$$F_{\text{box}} = A_{\text{box}} L + BL^2 \quad (6)$$

where A_{box} and B are given by Eqs. (4) and (5), respectively.

Now consider the case of an ideal polymer confined to a slit of height h . Retaining only the last term of Eq. (2)

and choosing $L_x = L_y \rightarrow \infty$ and $L_z = h$, the confinement free energy is given by $F_{\text{id,slit}}/k_{\text{B}}T = \pi^2 LP/3h^2$. This expression is expected to be valid for a worm-like chain in the limit where $P \ll h$. In the opposite limit where $h \ll P$, the chain is in the Odijk regime. Here, the exact expression for the free energy is given by³⁷ $F_{\text{id,slit}}/k_{\text{B}}T = 1.104L(P/h^2)^{-1/3}$. The intermediate regime between these two limiting cases is well approximated by an interpolation obtained by Chen and Sullivan,³⁸ who solved the worm-like chain diffusion equation in a slit geometry with hard-wall boundary conditions imposed at the slit surfaces. Their result is well approximated by the analytical expression

$$\frac{F_{\text{id,slit}}}{k_{\text{B}}T} = A_{\text{slit}}L, \quad (7)$$

where

$$A_{\text{slit}} = \frac{\pi^2}{3} \frac{P}{h^2} \left(5.14 \left(\frac{P}{h} \right)^2 + 1.98 \left(\frac{P}{h} \right) + 1 \right)^{-2/3}. \quad (8)$$

For sufficiently small h , excluded-volume interactions are negligible. Thus, Eq. (7) is approximately the difference in the conformational free energy of a slit-confined real chain and an unconfined ideal chain.

A polymer whose contour spans two nanopits can be viewed as two contour clusters, each centered on a single pit and connected with a linking strand that contributes a spring free energy, F_{spr} . As in Refs. 28 and 29, we approximate this free energy with a modified form of the Marko-Siggia force equation that accounts for the effects of vertical confinement in the nanoslit and was obtained from a parameterization of MC simulation data:³⁹

$$\frac{F_{\text{spr}}}{k_{\text{B}}T} = \frac{l^2}{2PL_s} \frac{D_{\text{eff}} - 1}{4(L_s - l)} [2L_s D_{\text{eff}} - l(D_{\text{eff}} + 1)] \quad (9)$$

Here, L_s is the contour length of the connecting strand, and the quantity l is the distance between the ends of the connecting strand, which for simplicity we choose here to be the spacing between the parallel edges of the nanopits. The effective dimensionality, D_{eff} , given by

$$D_{\text{eff}}(h) = 1 + \frac{2}{2 - \exp(-0.882(P/h)^{1.441})}, \quad (10)$$

interpolates between dimensions of 2 and 3 for small and large slit height, h , respectively. As in the original Marko-Siggia relation, this free energy only becomes appreciably larger than $k_{\text{B}}T$ when L_s is not significantly larger than l .

Now consider a polymer chain of contour length L that spans two nanopits of depth d , side length a , and spacing l . The total conformational confinement free energy of the polymer can be approximated

$$F_{\text{conf}} = F_{\text{cav}} - F_{\text{id,slit}} + F_{\text{spr}}, \quad (11)$$

where $F_{\text{id,slit}}$ is given by Eq. (7) and F_{spr} is given by Eq. (9). In addition, F_{cav} is the free energy increase

associated with confinement of parts of the polymer to the nanopits and is given by

$$F_{\text{cav}}(L_1, L_2) = F_{\text{box}}(L_1) + F_{\text{box}}(L_2), \quad (12)$$

where F_{box} is given by Eq. (6). The first term accounts for confinement of one subchain of length L_1 in one nanopit and another subchain of length L_2 in the other nanopit. Combining Eqs. (6), (11) and (12), it can be shown that

$$\frac{F_{\text{conf}}}{k_{\text{B}}T} = -A(L_1 + L_2) + B(L_1^2 + L_2^2) + F_{\text{spr}}(L_s) \quad (13)$$

where

$$A \equiv A_{\text{slit}} - A_{\text{box}}. \quad (14)$$

Defining $\lambda_1 \equiv L_1 + L_2$ and $\lambda_2 \equiv L_1 - L_2$, i.e., the sum of and the difference in the contour lengths in each of the nanopits, Eq. (13) can be written:

$$\frac{F_{\text{conf}}(\lambda_1, \lambda_2)}{k_{\text{B}}T} = -A\lambda_1 + \frac{1}{2}B\lambda_1^2 + \frac{1}{2}B\lambda_2^2 + F_{\text{spr}}(L - \lambda_1), \quad (15)$$

where we note the argument $L_s = L - \lambda_1$ in the last term. Equation (15) can be written

$$\frac{F_{\text{conf}}(\lambda_1, \lambda_2)}{k_{\text{B}}T} = \frac{\kappa_s}{2}(\delta\lambda_1)^2 + \frac{\kappa_a}{2}(\lambda_2)^2 + \mathcal{O}(\delta\lambda_1^3). \quad (16)$$

Here, $\delta\lambda_1 \equiv \lambda_1 - \lambda_1^{(\text{min})}$ and $(\lambda_1, \lambda_2) = (\lambda_1^{(\text{min})}, 0)$ is the location of the free energy minimum. The quantities κ_s and κ_a are effective spring constants that govern the fluctuations in the sum and difference of the contour lengths in the two pits, which are symmetric and asymmetric modes, respectively. Note that $\kappa_a = B$. The other coefficient, κ_s , does not have a cromulent closed-form expression in terms of the system parameters. However, in the limit of sufficiently small λ_1 , the spring free energy term in Eq. (16) is negligible. In this case, Eq. (15) can be rewritten:

$$F/k_{\text{B}}T \approx \frac{1}{2}B(\lambda_1 - A/B)^2 + \frac{1}{2}B(\lambda_2)^2 + \text{const} \quad (17)$$

Comparing Eqs. (17) and (16), it follows that $\kappa_s = \kappa_a$ and $\lambda_1^{(\text{min})} = A/B$.

In the simulations, we employ semiflexible polymer chains composed of N spherical monomers of diameter and fixed bond length both equal to w . Note that this is also the width of the chain. Since all quantities of distance are given in units of w , L_1 and L_2 are numerically equal to N_1 and N_2 , the number of monomers whose centers lie in the nanopits, and $\lambda_1 = N_1 + N_2$ and $\lambda_2 = N_1 - N_2$ are the sum and the difference of the number of monomers in the two pits. Likewise, $N_s = N - (N_1 + N_2) = N - \lambda_1$ is the number of monomers that lie outside the pits. Finally, note that the coefficients in Eqs. (15) and (16) have the following dependencies:

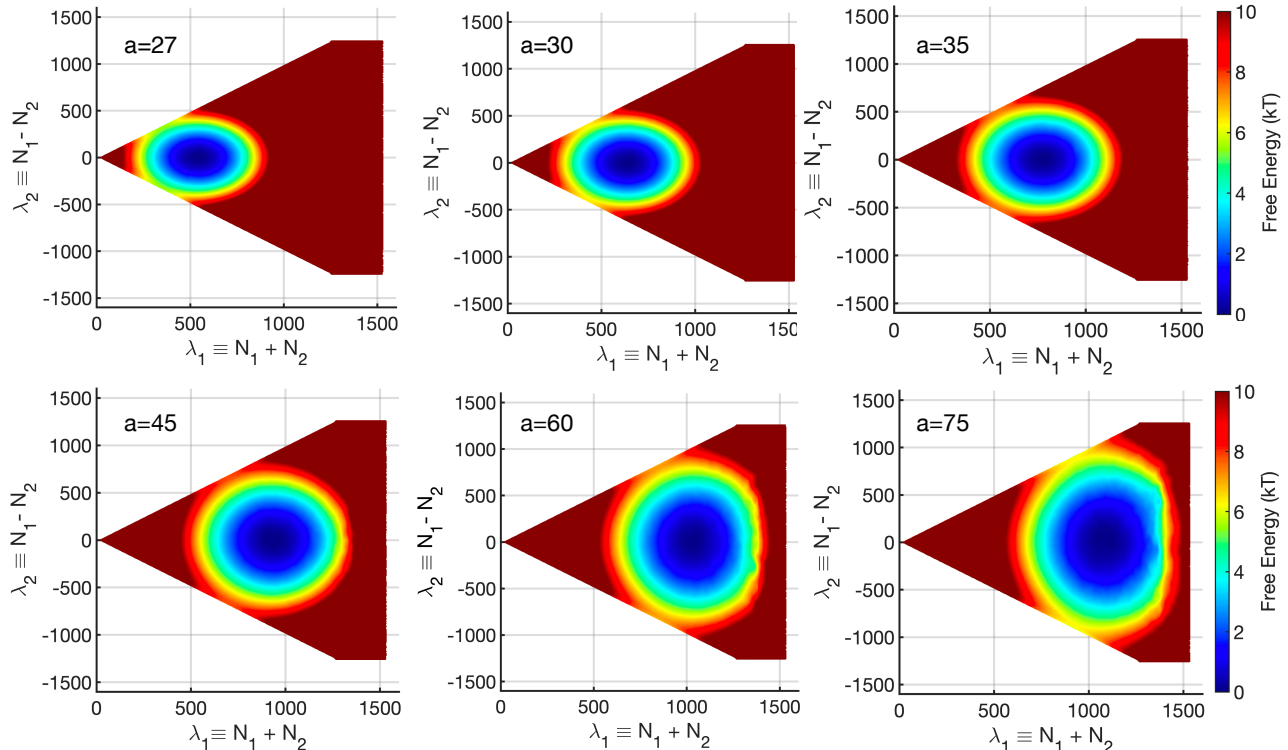


FIG. 2. Free energy vs $\lambda_1 \equiv N_1 + N_2$ and $\lambda_2 \equiv N_1 - N_2$. Results are shown for a polymer of length $N = 1600$ and bending rigidity $\kappa = 5$. In addition, the confining geometry is defined by slit height $h = 10$, pit depth $d = 20$, and pit spacing $l = 60$. Results are shown for various values of the pit side length, a . For visual clarity, the free energy is truncated at $10k_B T$.

$A = A(a, d, P, h)$ and $B = B(d, a)$. The dependence on polymer width w is omitted since this is the unit of length employed in this study.

For fixed $\lambda_1 = \lambda_1^{(\min)}$, (i.e., $\delta\lambda_1 = 0$) the free energy varies as

$$\frac{F_{\text{conf}}(\lambda_2)}{k_B T} = \frac{\kappa_a}{2} (\lambda_2)^2, \quad (18)$$

where

$$\kappa_a = B = \frac{\pi w}{4da^2}. \quad (19)$$

However, at $\lambda_2 = \lambda_2^{(\min)} = 0$,

$$\frac{F_{\text{conf}}(\lambda_1)}{k_B T} = \frac{\kappa_s}{2} (\delta\lambda_1)^2 + \mathcal{O}(\delta\lambda_1^3). \quad (20)$$

Equations (18) and (20) will be useful for comparison with the simulation data.

V. RESULTS

We begin with an examination of the effects of the cavity side length, a on the free energy functions. Note that

this was a key focus in the experimental study of Ref. 28. Figure 2 shows a collection of graphs of the free energy, $F(\lambda_1, \lambda_2)$, where λ_1 and λ_2 are the sum and difference of the number of spherical monomers in the nanopits, respectively. Results are shown for a system composed of a polymer of length $N = 1600$ monomers and persistence length of $P = 5$ confined in a slit of height $h = 10$. The two nanopits embedded in one of the slit surfaces have a depth of $d = 20$ and spacing $l = 60$. The individual graphs show results for various values of the nanopit side length, a , ranging from $a = 30$ to $a = 90$. The qualitative trends are straightforward. In all cases, the free energy minimum is centered at a point with $\lambda_2 = 0$, which implies that the most probable configuration is one in which $N_1 = N_2$, i.e., an equal number of monomers located in each pit. The value of $\lambda_1^{(\min)}$ increases gradually with increasing a . This implies that $\lambda_1 \equiv N_1 + N_2$, the total number of monomers located in the two pits, increases as the pit width increases. This follows from the fact that larger pits can more comfortably accommodate larger numbers of monomers since the impact of the excluded volume interactions, determined by the coefficient B , defined in Eq. (5), decreases as the cavity volume increases.

Figure 3(a) shows the cross section of the free en-

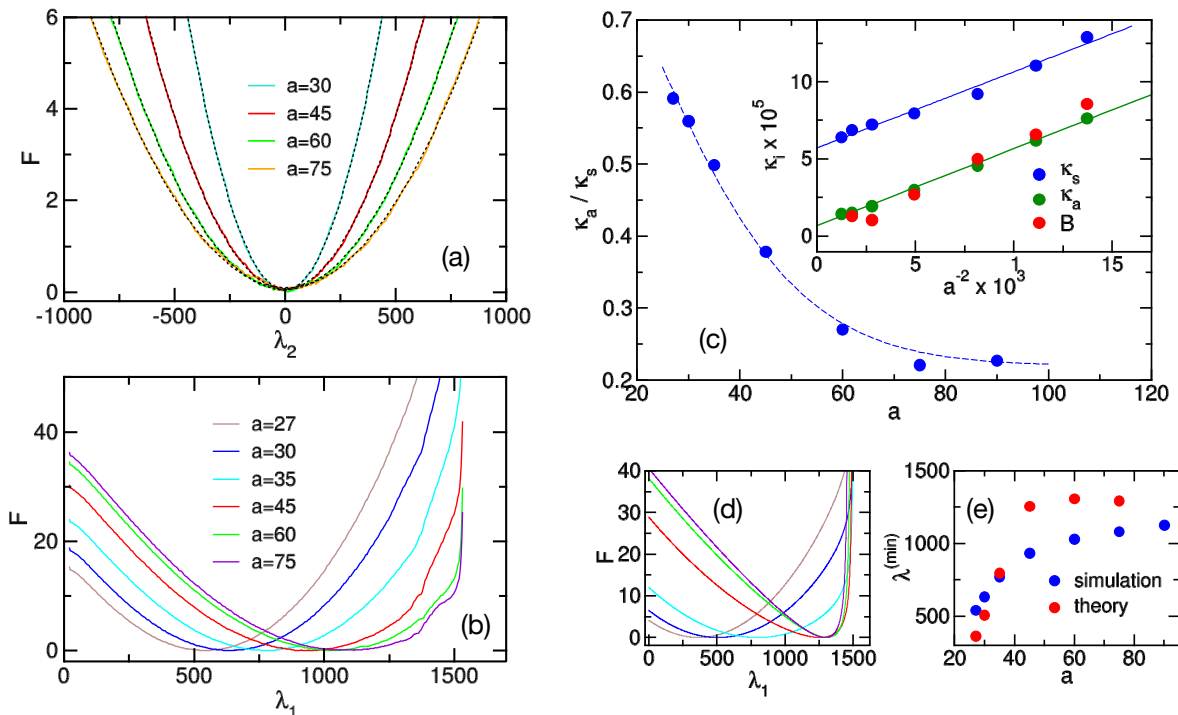


FIG. 3. (a) F vs λ_2 for fixed $\lambda_1 = \lambda_1^{(\min)}$. The results were obtained from a cross sections of the 2D free energy functions of Fig. 2. As in Fig. 2, $N = 1600$, $\kappa = 5$, $h = 10$, $d = 20$, and $l = 60$. The dotted lines show quadratic fits to the data. (b) F vs λ_1 for fixed $\lambda_2 = 0$. (c) The inset shows the variation of κ_s and κ_a with a^{-2} . Here, κ_a and κ_s are the coefficients obtained for fits to $F(\lambda_2; \lambda_1 = \lambda_1^{(\min)})$ and $F(\lambda_1; \lambda_2 = 0)$, respectively. Solid lines show fits using the $F = \gamma_0 + \gamma_1 a^{-2}$. The data were obtained from fits to the data in Fig. 3, as described in the text. Overlaid on the data are estimates for the excluded-volume coefficient B (see Eq. (6)) obtained from calculations of the confinement free energy of a single polymer chain in a rectangular box with the same dimensions as the nanopits, as described in the text. The main part of the figure shows the variation of the ratio κ_a/κ_s with pit side length a . The dashed line is a guide for the eye and was calculated using the function $\kappa_a/\kappa_s = 0.22 + 0.608e^{-((a-10)/28.39)^{1.5}}$. (d) Predicted F vs λ_1 using Eq. (15). The colors for the curves for the values of a are the same as in (b). (e) Variation of $\lambda_1^{(\min)}$ with a determined from the free energy functions shown in (b) and the theoretical curves shown in (d).

ergy through the free energy minimum along the λ_2 axis. As predicted by Eq. (18), the free energy exhibits a quadratic dependence on λ_2 . Indeed the fits of each curve to the function $F = c_1(\lambda_2)^2$, shown as the dotted lines in the figure, are in excellent agreement with the data. The effective spring constant can be evaluated using $\kappa_a = 2c_1$. Figure 3(b) shows the cross section of the free energy through the free energy minimum along the λ_1 axis. The shift in the minimum to higher λ_1 as the pit width a increases is evident. The free energy curves in Fig 3(a) were fit to the polynomial, $F(\lambda_1) = c_2(\lambda_1 - \lambda_1^{(\min)})^2 + c_3(\lambda_1 - \lambda_1^{(\min)})^3$, in the vicinity of the free energy minimum and used to obtain the effective spring constant, $\kappa_s = 2c_2$.

The inset of Figure 3(c) shows that the κ_a values extracted from the fits scale roughly linearly with a^{-2} . This scaling is qualitatively consistent with the prediction of Eq. (19). In the limit of large pit width (i.e., small a^{-2}), κ_a appears to deviate from the linear curve and approach a finite value. A fit of these data (exclud-

ing the data point for the largest a value) to the function $F = \gamma_0 + \gamma_1 a^{-2}$ yields $\gamma_0 = (6.6 \pm 0.9) \times 10^{-6}$ and $\gamma_1 = 0.050 \pm 0.001$. By comparison, Eqs. (18) and (19) predict a linear variation of F with respect to a^{-2} with zero intercept and slope of $\pi w/(4d) = 0.039$. This value is in close agreement with the measured value of γ_1 .

In order to further assess the observed variation of κ_a with a^{-2} , we carry out a complementary simulation to measure the confinement free energy of a polymer trapped in a box of dimensions $a \times a \times d$. We follow the approach taken in a previous study,⁴⁰ which differs from that used in the rest of the study; details of the calculation are presented in Appendix B. The simulations provide an estimate of the variation of the confinement free energy with respect to polymer length for a polymer with the same bending rigidity ($\kappa = 5$) as used in the two-pit simulations. For sufficiently long polymers the free energy is expected to vary with contour length according to Eq. (6). Fitting the data with $F(m) = A + Bm^2$, where m is the polymer length, yields

values of the virial coefficient, B . As noted earlier, the effective spring constant for the contour-length difference is expected to satisfy $\kappa_a = B$. Overlaid on the data in the inset of Fig. 3(c) are the values of B calculated using this approach. The values of κ_a and B are in reasonable agreement over the range of a examined. The small discrepancies arise mainly from the fact that the nanopit is partially “open” in the slit portion of the geometry in contrast to the fully enclosed box used to estimate B . The results of this calculation show that the theoretical model presented in Section II accounts for the variation of F with λ_2 .

As noted in Section IV, when the contour length of that portion of the polymer located outside the nanopits is sufficiently large (i.e., low λ_1) then the spring free energy of Eq. (9) is negligible. In this case, the confinement free energy of Eq. (16) can be approximated by Eq. (17), implying that $\kappa_s = \kappa_a$. The variation of the measured value of κ_s with a^{-2} shown in the inset of Fig. 3(c) clearly shows that this is not correct. Instead, κ_s is consistently greater than κ_a for all a . Restricting the fit to smaller values of λ_1 well below $\lambda_1^{(\min)}$ where the spring free energy F_{spr} of Eq. (9) is expected to be negligible does not significantly change the results. Like κ_a , the coefficient κ_s does appear to vary roughly linearly with a^{-2} , but the two coefficients are offset by roughly $\Delta\kappa \equiv \kappa_s - \kappa_a \approx 5 \times 10^{-5}$ for the entire range of a examined here. The main part of Fig. 3(c) shows the variation of the ratio κ_a/κ_s with respect to pit side length a . The ratio decreases rapidly at low a and appears to asymptotically approach ≈ 0.2 at larger a . Figure 3(d) shows the predicted variation of F with λ_1 (for $\lambda_2 = 0$) using Eq. (15). The qualitative trends are comparable to those in Fig. 3(b), most notably the shift in the location of the minimum, $\lambda_1^{(\min)}$, to higher values as the cavity width increases. However, these values tend to underestimate the measured values at low a and overestimate them at higher a , as is clearly shown in Fig. 3(e).

It is useful to compare our simulation results with those of Ref. 28. Note that the experiments and simulations in that work did not measure the free energy directly as in the present study, but rather analyzed the dynamics of the fluctuations in λ_1 and λ_2 . However, the correlation times for the fluctuations are closely related to the two effective spring constants. The spring constant κ_a governs the fluctuations in the back-and-forth trading of polymer contour between the two nanopits. As noted in Ref. 28 the correlation time in the fluctuations is expected to satisfy $\tau_a = \xi/\kappa_a$, where ξ is the hydrodynamic drag on the chain. This implies that $\tau_a \propto a^2$. Klotz *et al.* measured τ_a for λ DNA in the same complex confinement geometry modeled in the present work, and the data are roughly consistent with the predicted quadratic dependence of τ_a with a (see Fig. 5(a) of Ref. 28).

The spring constant κ_s governs the fluctuations in the total contour trapped in the two pits, whose correlation time is expected to vary as $\tau_s = \xi/\kappa_s$. Consequently, the ratio of correlation times should satisfy $\tau_s/\tau_a = \kappa_a/\kappa_s$.

The ratio of κ_a/κ_s is roughly consistent with the measured variation of τ_s/τ_a for λ DNA (see Fig. 5(c) in Ref. 28). At $a = 30$ the ratio curvature-constant ratio is about $\kappa_a/\kappa_s \approx 0.56$ and appears to level off at around $a \approx 60$. For DNA with an effective width of 10 nm, these correspond to $a = 300$ nm and $a = 600$ nm, respectively. In Ref. 28 the correlation-time ratio τ_s/τ_a is about 0.62 at $a = 300$ nm, and the curve appears to level off at about $a = 500$ nm. Thus, there is decent quantitative agreement between our simulations and experiment. On the other hand, κ_a/κ_s appears to approach approximately 0.22 at large a , while the limiting value in the experiments is just below 0.1. The quantitative discrepancies could arise from the implicit neglect of the $\mathcal{O}(\lambda^3)$ correction terms in the approximation $\kappa_a/\kappa_s = \tau_s/\tau_a$. In addition, note the contour length of the model polymer chain of $N = 1600$ corresponds to a contour length of $L_c = 1600w$. For an effective width of $w = 10$ nm, this corresponds to $L_c = 16 \mu\text{m}$, slightly shorter than the value of $L_c = 16.5 \mu\text{m}$ of λ DNA and even shorter still than the contour length of λ DNA stained with YOYO-1 dye at a 10:1 base-pair/dye ratio, which is expected to increase L_c by roughly 15%.⁴¹ The small but significant difference between the experimental and simulation values of L_c/w may also account for the discrepancies in the data.

The simulations carried out in Ref. 28 used a semiflexible chain of spherical beads interacting with the Weeks-Chandler-Anderson (WCA) particles connected by a finitely extensible nonlinear elastic spring potential with model parameters set as in Ref. 42. In addition a three-particle harmonic potential was used to impose bending rigidity with a persistence length of $P \approx 5w$. Although the details differ this model is very similar in effect as the semiflexible hard-sphere chain in the present study. On the other hand, to make the simulations computationally feasible, the contour length ($L_c/w \approx N=100\text{--}300$ monomers) was significantly shorter than the value here ($L_c/w = N=1600$ monomers), and shorter still than the experimental value. Likewise, the values of the various confinement geometry parameters (slit height and cavity depth, side length, and separation distance) were also significantly smaller (measured in units of w) than the experimental values, as noted by the authors of the study. In spite of these limitations, variation of the values of τ_s/τ_a with respect to a measured in the simulations were in decent quantitative agreement with the experimental values and the theoretical predictions of Eq. (15), as well as the results of our simulations. We speculate that the choice of the confinement dimensions to compensate for the artificially short polymer chains used in the simulations of Ref. 28 in effect produced a free-energy landscape comparable to that calculated for our model as well as the one for the experimental system. What has emerged from our simulations, however, is that this cannot be taken as corroboration of the theoretical model for the free energy whose predictions yield such significant quantitative discrepancies with our results.

The other geometric parameter that was varied in the

experiments of Ref. 28 was the spacing l between the two nanopits. Klotz *et al.* found that the asymmetric mode correlation time, τ_a increased linearly with l with a rate that increased with the nanopit width, a . This is consistent with a prediction that assumes $\tau_a = \xi/\kappa_a$, where $\kappa_a = w/a^2d$ is independent of l , and that the friction coefficient satisfies $\xi = \alpha\eta l + \epsilon$, where α is a numerical proportionality factor, η is the buffer viscosity and ϵ is an offset factor. The latter assumption invokes the blob model for the linking strand, with the result that the stretched linking strand length is proportional to l . While our MC simulations cannot be used to evaluate the validity of the assumed behavior of ξ , they can be used to test the assumed independence of κ_a to l . Figure 4(a) shows the F vs λ_2 free energy cross sections for various l with the other geometric parameters fixed to $a = 60$, $d = 20$ and $h = 10$. As in Fig. 3(a), the functions vary quadratically with λ_2 . Fitting the data yields the effective spring constant κ_a for each curve. Figure 4(b) shows the variation of κ_a with l over the range $l = 30 - 90$. A linear fit of the data yields a slope of $(1.3 \pm 0.8) \times 10^{-8}$. Thus, our results do not show any statistically significant variation in κ_a with cavity spacing, thus validating the assumption employed in the analysis of the experimental data.

Figure 4(c) shows the effect of varying l on the F vs λ_1 free energy cross sections. The main trend is the shift of $\lambda_1^{(\min)}$ to lower λ_1 as the cavity spacing increases. This follows trivially from the fact that increasing l increases the linking strand length and so decreases the total polymer contour that available to occupy the two cavities. Figure 4(d) shows the predicted curves using Eq. (15). While the reduction in $\lambda_1^{(\min)}$ with increasing l is observed, the trend is much weaker in the prediction. This is especially clear in the inset of the figure which compares the simulation and theoretical values of $\lambda_1^{(\min)}$. Thus, as was the case for the variation of the cavity width, Eq. (15) yields qualitatively correct but quantitatively poor predictions for F vs λ_1 , while yielding quantitatively accurate results for F vs λ_2 .

Although the experimental study of Ref. 28 characterized the trends of varying only the cavity width and spacing, it is of interest here to examine the effects of varying other system parameters. We choose the cavity depth parameter D , slit spacing h , as well as the polymer persistence length, P . Our results serve as predictions for any future experiments that may examine such effects. In addition, they provide further tests for the predictions of the theoretical model of Section IV.

We consider first the effect of changing D , the pit depth as measured from the embedding surface. Figure 5(a) shows free energy cross sections $F(\lambda_2)$ for several values of D with fixed $h = 10$, $a = 60$, and $l = 60$. The dotted lines are parabolic fits to $F(\lambda_2)$, from which the coefficient κ_a has been extracted. The parabolas in Fig. 5(a) widen slightly with increasing D . Correspondingly, κ_a increases monotonically with d^{-1} , where $d = h + D$, as shown in Fig. 5(b). A linear fit of κ_a vs d^{-1} yields a

slope of $(1.9 \pm 0.3) \times 10^{-4}$. Equation (19) predicts a linear variation with a slope $\pi w/(4a^2) = 2.2 \times 10^{-4}$, which is comparable to the measured value.

Figure 5(c) shows the effect of varying D (through variation of D at fixed h) on the cross section $F(\lambda_1)$. The principal effect is that the minimum value $\lambda_1^{(\min)}$ increases with D . This effect is due to the fact that increasing d increases that cavity volume, thus making it easier to accommodate a greater portion of the polymer contour. This is exactly the same explanation for the qualitative trend for varying a in Fig. 3(b). As in that case, however, shift of the curves to lower λ_1 as the cavity volume increases are only qualitatively consistent with the theoretical predictions shown in Fig. 5(d).

Another way of varying d , and thus the pit volume, is adjusting the slit height h while keeping the cavity depth D fixed. Figure 6(a) shows the effect of such a variation on the cross section $F(\lambda_2)$. Increasing h widens the parabolas. A fit to parabolic functions provides estimates of the coefficient κ_a , which is plotted in Fig. 6(b) as a function of d^{-1} . A fit of the data yields a slope of $(2.8 \pm 0.4) \times 10^{-4}$, which is in good agreement with the prediction from Eq. (19) of $\pi w/(4a^2) = 2.2 \times 10^{-4}$. Figure 6(c) shows the effect of varying the slit height on the cross section $F(\lambda_1)$. Increasing h reduces $\lambda_1^{(\min)}$, the most probable value of the total polymer contour in the pits. The theoretical predictions for F vs λ_1 shown in Fig. 6(d) again show the correct qualitative trend, in this case decreasing $\lambda_1^{(\min)}$ with increasing h , though with significant quantitative discrepancies with the curves obtained from the simulations.

Finally, we examine the effects of varying the polymer persistence length on the free energy functions. Figure 7 shows results for varying the polymer bending rigidity, κ , for a system with $a = 60$, $d = 20$ and $h = 10$. As in previous calculations, the F varies quadratically with λ_2 , as shown in Fig. 7(a). Values of the effective spring constant κ_a were obtained from fitting the data and are shown in Fig. 7(b). There is a rapid initial reduction in κ_a until about $\kappa \approx 2.5$, after which κ_a remains relatively constant. The invariance of κ_a with respect to κ is consistent with the prediction of Eq. (19), which has no dependence on P . The deviation from this result at very low κ may be due to the neglect of higher order terms in the virial expansion of F_{box} (see Eq. (6)), which are expected to become more significant with increasing the polymer flexibility.

As is evident in Fig. 7(c), varying the bending rigidity has a pronounced effect on the F vs λ_1 curves. Interestingly, the position of the minimum does not vary monotonically with κ . As is clearer in the inset of Fig. 7(d), $\lambda_1^{(\min)}$ initially increases with κ , reaches a maximum at about $\kappa = 5$ and then decreases. Figure 7(d) shows theoretical predictions calculated using Eq. (15). Only curves for $\kappa=2.5$, 5 and 7.5 are shown. For $\kappa \gtrsim 8$ the theory fails completely as the coefficient A defined in Eq. (14) becomes negative because $A_{\text{slit}} < A_{\text{box}}$, where these two

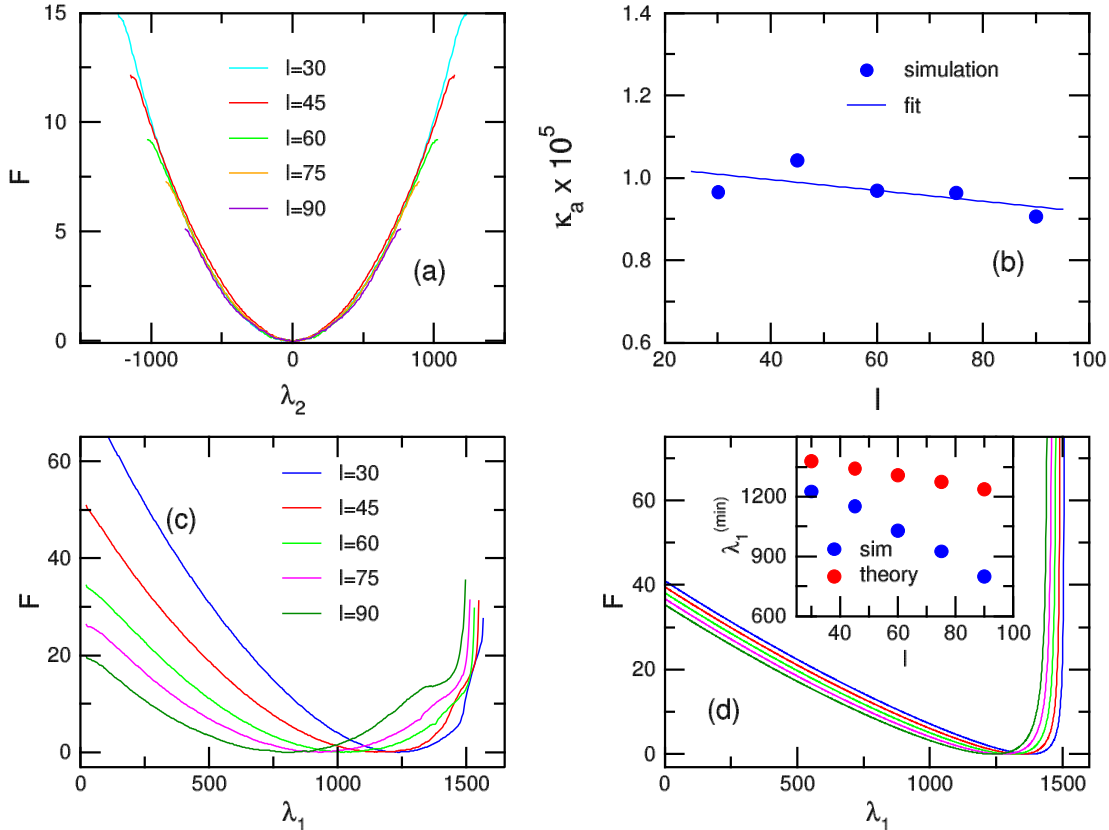


FIG. 4. Effects of varying the cavity separation, l . Results are shown for fixed $a = 60$, $h = 10$, $d = 20$, $\kappa = 5$, and for several values of l . (a) Free energy vs λ_2 for fixed $\lambda_1 = \lambda_1^{(\min)}$. (b) Variation of κ_a with l . The values of κ_a were obtained from fits to the curves in (a). (c) Free energy vs λ_1 for fixed $\lambda_2 = 0$. (d) Prediction of F vs λ_1 using Eq. (15). The inset shows the variation of $\lambda_1^{(\min)}$ with l for the free energies obtained from simulations and the theory.

quantities are defined in Eq. (8) and Eq. (4), respectively. A likely cause of this problem is the expression for A_{box} in Eq. (4) is strictly only valid for $P \ll d$ and $P \ll a$, conditions that break down as the bending rigidity increases.

VI. CONCLUSIONS

In this study we have used MC simulations to measure a 2D free-energy landscape for a polymer confined to a complex geometry consisting of a slit with two cavities embedded in one of the surfaces. The simulation results were used to critically evaluate the theoretical model used to interpret the results of an experiment that examined the physical behavior of a λ DNA molecule confined to this geometry.²⁸ The values of parameters that define the lengthscales in the simulations for both the confining geometry and the polymer were chosen to be close to the lengthscales in the experiments. The free energy was calculated as a function of the sum, λ_1 , and difference, λ_2 ,

of the polymer contour length in the two cavities, and for convenience the analysis focused on the cross sections of F along one variable through the minimum of the other. The theoretical model is constructed using established results for the confinement free energy of polymers in cavities and slits.

We observe a marked difference in the accuracy of the theoretical predictions for the λ_1 and λ_2 cross sections. We find the predictions for $F(\lambda_2)$ are quantitatively accurate upon variation of every confining geometry length-scale, as well as the polymer persistence length. By contrast, we find only qualitative agreement for $F(\lambda_1)$ and appreciable quantitative discrepancies. The origin of the quantitative discrepancy for the case of λ_1 in part lies in the simplistic, if convenient, modeling of the surface-embedded cavities as enclosed boxes. In most of the simulations (as well as in the experiments) half of the cavity height (i.e. the distance from the cavity bottom surface to the other slit surface) is open to the slit such that the polymer is not completely confined in the lateral dimension. Further, the simple analytical expression for

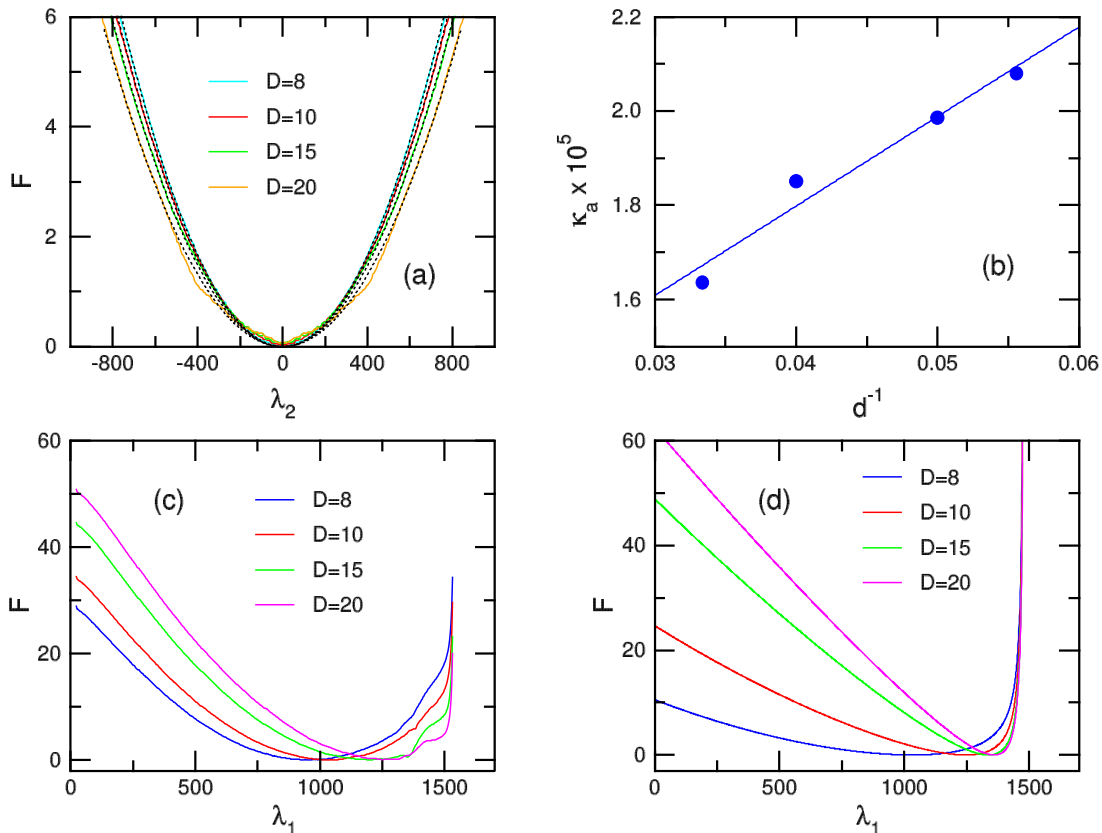


FIG. 5. Effects of varying the cavity depth, D . Results are shown for fixed $a = 60$, $h = 10$, $l = 60$, $\kappa = 5$, and for several values of D . (a) Free energy vs λ_2 for fixed $\lambda_1 = \lambda_1^{(\min)}$. (b) Variation of κ_a with $d^{-1} \equiv (h + D)^{-1}$. The values of κ_a were obtained from fits to the curves in (a). (c) Free energy vs λ_1 for fixed $\lambda_2 = 0$. (d) Prediction of F vs λ_1 using Eq. (15).

the cavity confinement free energy likely exhibits finite-size effects for cavities as small as employed here. For example, it was noted that F_{box} fails for longer persistence lengths because of the requirement that P be much smaller than the cavity dimensions. The failure of the theoretical model to provide quantitatively accurate predictions for λ_1 is less surprising than its success in doing so for λ_2 . Apparently the effects of some of the model inaccuracies cancel out for this case.

Our study provides a useful lesson on the limitations of using simplistic (if convenient) analytical expressions for polymer free-energy landscapes to interpret experimental data and points to the value of carrying out accurate (if time consuming) calculations of the free energy instead. The apparent agreement of the experimental (and even Langevin dynamics simulation) results of Ref. 28 with the theoretical predictions suggested a theory that was much better than was revealed in our study. In future work, we will carry out similar calculations of free-energy landscapes for comparable complex geometries that have been employed in other experiments using DNA.^{14,23–28,30,31} Such calculations should contribute to

the future development of confinement-based nanotechnologies for the manipulation and analysis of DNA and other polymers.

ACKNOWLEDGMENTS

This work was supported by the Natural Sciences and Engineering Research Council of Canada (NSERC). We are grateful for the advanced computing resources provided by the Digital Research Alliance of Canada as well as ACENET, their regional partner in Atlantic Canada. Finally, we would like to thank Alex Klotz for helpful discussions.

Appendix A: Implementation of the WHAM2D method: further details

As noted in Section III, the WHAM2D method is used to calculate the two-dimensional free-energy function $F(\lambda_1, \lambda_2)$ for the confined-polymer model of this

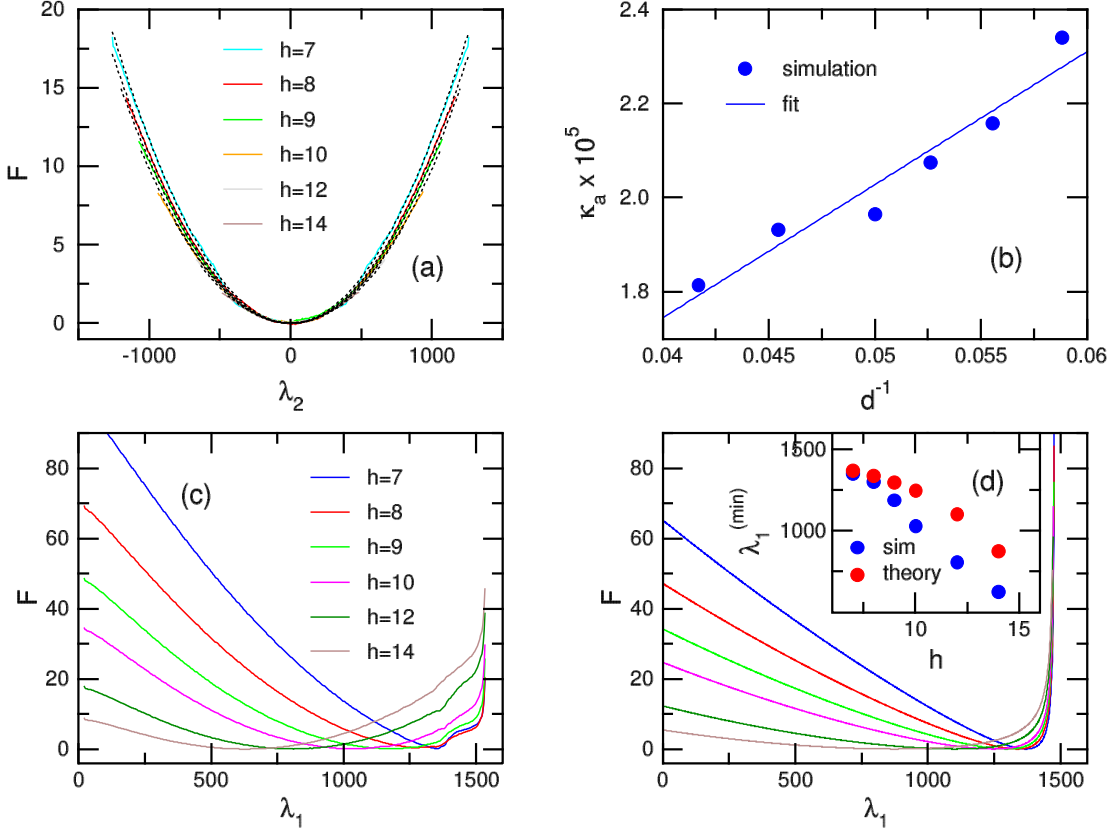


FIG. 6. Effects of varying the slit height, h . Results are shown for $a = 60$, $D = 10$, $l = 60$, and $\kappa = 5$. (a) F vs λ_2 for $\lambda_1 = \lambda_1^{(\min)}$. The dotted lines are quadratic function fits to the calculated curves. (b) Variation of κ_a , extracted from the fits in (a), with respect to d^{-1} , where $d = h + D$. The dashed line is a linear fit to the data. (c) F vs λ_1 for $\lambda_2 = 0$. (d) Prediction of F vs λ_1 using Eq. (15). The inset shows the variation of $\lambda_1^{(\min)}$ with h for the free energies obtained from simulations and the theory.

study. In this appendix we provide further detail regarding the implementation of the method.

The free energy is measured as a function of the sum (λ_1) and the difference (λ_2) of the polymer contour contained within each of the two nanopits of the confinement geometry. The function can be written $F(\lambda_1, \lambda_2) = -k_B T \ln \mathcal{P}(\lambda_1, \lambda_2)$, where $\mathcal{P}(\lambda_1, \lambda_2)$ is the probability distribution associated with the two variables. While a single simulation can in principle be used to estimate $\mathcal{P}(\lambda_1, \lambda_2)$ (and therefore also $F(\lambda_1, \lambda_2)$), regions of high free energy have a low probability and are therefore subject to infrequent sampling and thus poor statistical accuracy.

Multiple-histogram umbrella sampling methods such as WHAM2D offer a straightforward means to overcome this problem. The basic idea is to carry out a collection of simulations, each of which employs a unique biasing potential designed to ensure that the system samples a particular region of the free-energy landscape. WHAM2D uses two-dimensional harmonic potential energy func-

tions of the following form:

$$U_b = \frac{1}{2}k_1(\lambda_1 - \lambda_1^{(c)})^2 + \frac{1}{2}k_2(\lambda_2 - \lambda_2^{(c)})^2, \quad (\text{A1})$$

where the biasing energy minimum is located at $\lambda_1 = \lambda_1^{(c)}$ and $\lambda_2 = \lambda_2^{(c)}$. (Here we employ the notation relevant to the model system of the present study.) The system tends to sample regions near the energy minimum over a range that depends on the biasing potential constants k_1 and k_2 . Sampling λ_1 and λ_2 yields a two-dimensional histogram for the biased system. When using the WHAM2D method, a collection of histograms, each calculated using a biasing potential with a unique choice of $\lambda_1^{(c)}$ and $\lambda_2^{(c)}$, is calculated. The WHAM2D algorithm uses these histograms to reconstruct the underlying unbiased probability distribution, $\mathcal{P}(\lambda_1, \lambda_2)$. (In practice, the algorithm uses as input the histories of λ_1 and λ_2 that are produced by the MC program, from which such histograms are calculated.) The details of the histogram reconstruction algorithm can be found

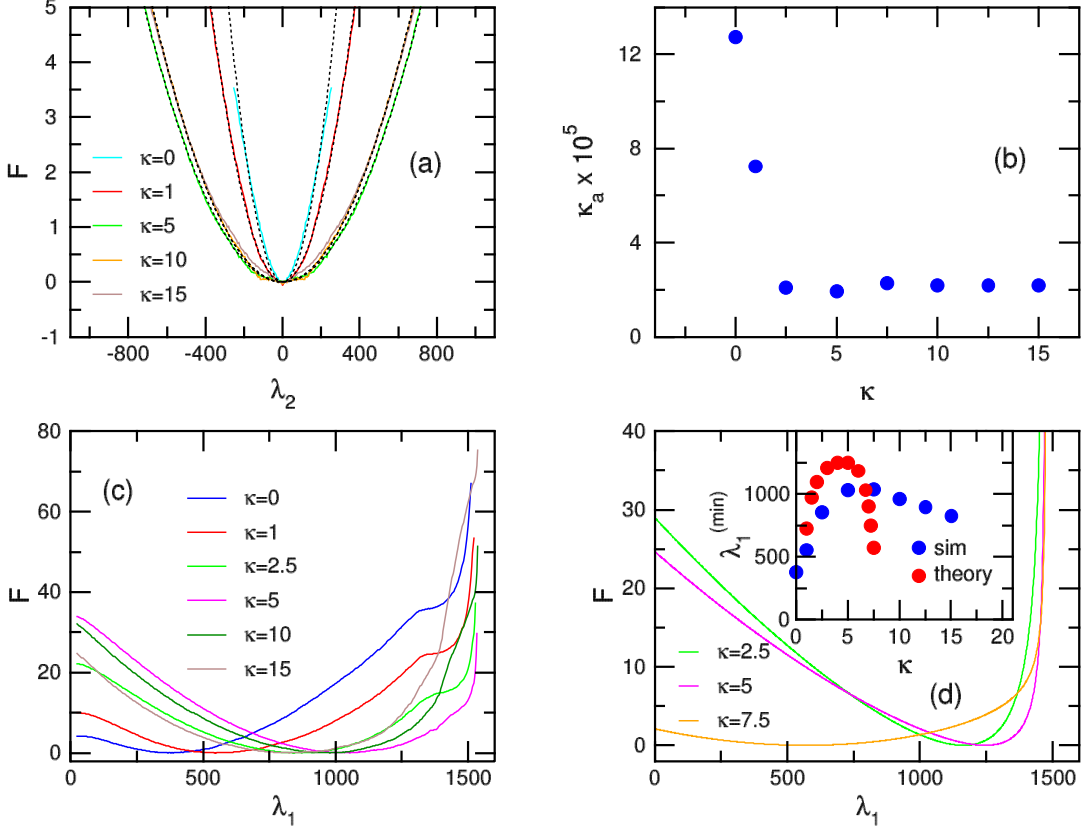


FIG. 7. Effects of the variation of the polymer bending rigidity, κ . Note that increasing κ corresponds physically to increasing the persistence length. Results are shown for fixed $a = 60$, $d = 20$, $h = 10$ and $l = 60$. (a) F vs λ_2 for $\lambda_1 = \lambda_1^{(\min)}$. The dotted curves are quadratic fits to the data. (b) Effective spring constant, κ_a vs bending rigidity, where κ_a have been determined from the fits to the data in (a). (c) Variation of F with λ_1 . (d) Prediction of $F(\lambda_1)$ using Eq. (15). The inset shows the variation of $\lambda_1^{(\min)}$ with κ for both the simulation results and the theoretical predictions.

elsewhere.³²

A key consideration in the implementation of the method are the choices of the parameters k_1 and k_2 , as well as the “location” of the biasing potential, defined by $\lambda_1^{(c)}$ and $\lambda_2^{(c)}$. In order for the method to yield statistically sound results, it is essential that there be sufficient overlap of neighbouring histograms, i.e., those for nearest-neighbour locations of biasing potentials. This imposes a relationship between the spacing of the biasing potential locations and the parameters k_1 and k_2 . The biasing potential locations are chosen to be laid out on a rectangular grid in the $\lambda_1 - \lambda_2$ in a region over which the free energy is to be evaluated.

Figure 8(a) illustrates this approach for the confined-polymer model system. The triangular region is the domain over which the free energy is evaluated. (As noted in Sec. III, the definitions of λ_1 and λ_2 require that $\lambda_2 \in [-\lambda_1, \lambda_1]$, yielding such a triangular domain.) The evenly spaced circles in the figure represent equipotential lines for each biasing potential employed in the calcula-

tion. The centers of the circles (i.e. the centers of the potentials) are given by $\lambda_1^{(c)}$ and $\lambda_2^{(c)}$. The rectangular grid of potential centers are chosen only to lie in the domain of interest in the $\lambda_1 - \lambda_2$ plane. The spacings $\Delta\lambda_1$ and $\Delta\lambda_2$ along the λ_1 and λ_2 axes, respectively, are illustrated in the figure.

Figure 8(b) and (c) provides a visual description of the method using a one-dimensional example, for visual clarity. Figure 8(b) shows a collection of histograms calculated for a set of harmonic biasing potentials evenly spaced along the λ axis over a chosen range of λ . The potential spacing and the curvature constant of the biasing potential is chosen to ensure that the distributions overlap appreciably, an essential requirement for the WHAM and WHAM2D methods. The resulting distributions are used as input into the WHAM algorithm, which generates the probability histogram for the unbiased system shown as the blue curve in Fig. 8(c). The corresponding free-energy function, shown as the orange curve, is determined simply by $F(\lambda)/k_B T = -\ln \mathcal{P}(\lambda)$. Although

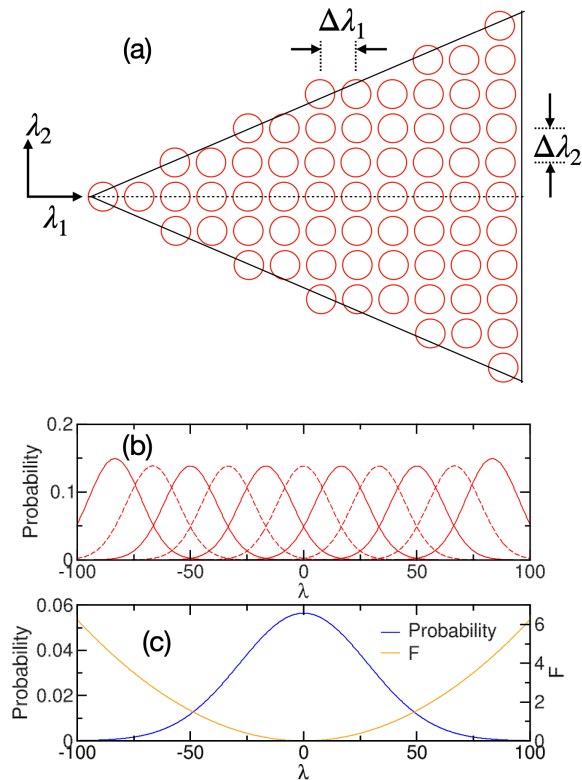


FIG. 8. (a) Schematic illustration of the implementation of the WHAM2D method for the model system. The triangle defines the region in the $\lambda_1 - \lambda_2$ plane over which the free energy is to be evaluated. Each red circle is associated with a two-dimensional harmonic biasing potential centered at the circle center, and represents a equipotential line for an energy of the order of $1 k_B T$. (b) 1D illustration of the WHAM technique. The figure shows a collection of overlapping histograms, each of which has been calculated in a simulation using a harmonic biasing potential centered at a unique position along the λ axis. Curves alternate between solid and dashed for visual clarity. (c) Probability histogram reconstructed from the histograms in (b) using the WHAM algorithm. The orange curve is the corresponding free energy profile, $F(\lambda)/k_B T = -\ln \mathcal{P}(\lambda)$.

Figs. 8(b) and (c) are 1D illustrations, the case for 2D is essentially the same. In that case, though, there is freedom to choose biasing potential curvature constants (k_1 and k_2) and lattice spacings for the biasing potentials ($\Delta\lambda_1$ and $\Delta\lambda_2$) that differ in the two dimensions.

Appendix B: Calculation of a semiflexible polymer confined to a rectangular cavity

In Section V, we examined the variation of the effective spring constant, κ_a , with the pit side length a . As

noted in Section IV the spring constant is expected to satisfy $\kappa = B$, where B is the virial coefficient appearing in Eq. (6) that accounts for the excluded-volume interactions in a semiflexible polymer confined to a rectangular box of dimension $a \times a \times d$. The coefficient B was calculated by measuring the variation of the free energy of such a confined polymer with respect to its contour length. The results for B , shown in Fig. 3(c) agree reasonably well with those for κ_a . In this appendix we present the method used in this calculation.

We follow the approach taken in Ref. 40. In essence, we measure the variation of the conformational free energy of a polymer that translocates through a narrow hole in a hard wall from a “semi-free” space on one side (*cis*) of the wall to a hard-walled box of dimensions $a \times a \times d$ on the other side (*trans*). In the case where m monomers of a N -monomer chain have translocated into the box, the free energy is $F_1(m) = F_{\text{trans}}^{(cw)}(m) - F_{\text{cis}}^{(w)}(N - m)$. The first term denotes the free energy of a chain of length m tethered to a wall (“w”) and confined to a cavity (“c”) on the *trans* side of the pore, i.e., into the cavity. A polymer that translocates through a pore in a barrier with no confinement on either side likewise has a free energy $F_0(m) = F_{\text{trans}}^{(w)}(m) - F_{\text{cis}}^{(w)}(N - m)$. We define the confinement free energy as $F_{\text{conf}}(m) = F_1(m) - F_0(m) = F_{\text{trans}}^{(cw)}(m) - F_{\text{trans}}^{(w)}(m)$. Thus, calculation of two translocation free energy functions, one with and one without cavity confinement on the *trans* side yields the confinement free energy. Note that this represents the change in the free energy required to confine a chain tethered at one end to a flat wall to cavity. However, as we have noted in a previous study⁴³ the free energy cost of localizing an end monomer to interior surface of a confining cavity is small. It is not expected to affect the calculation of B .

Translocation free energy functions for a chain of length $N = 500$ and bending rigidity $\kappa = 5$ were calculated with and without a rectangular confining cavity on one side, and the difference between the two was used to calculate $F_{\text{conf}}(m)$. As in Ref. 40 each free energy calculation employed the Self-Consistent Histogram (SCH) method.³⁴ This is essentially the equivalent of the 1D WHAM method, except that it uses square-well biasing potentials (“windows”) instead of quadratic functions. A set of 199 simulations were carried out, each a biasing potential window width of $\Delta m = 5$, centered on m values such that each window overlapped by half with adjacent windows. The simulations were each run for 5×10^8 MC cycles following an equilibration period of 2×10^7 MC cycles. Further details of the method can be found in Ref. 40.

Figure 9 shows F_{conf} vs m for a chain translocating into a rectangular box with various values of the side length, a . The dotted black lines overlaid on the curves show fits to the function $F = c_0 + c_1 m + B m^2$, which was carried out over the range of $m = 250 - 500$. The inset shows the functions $F_1(m)$ and $F_{\text{conf}}(m)$ for $a = 30$, as well as the translocation free energy function $F_0(m)$ in the case of no confinement on either side of the barrier.

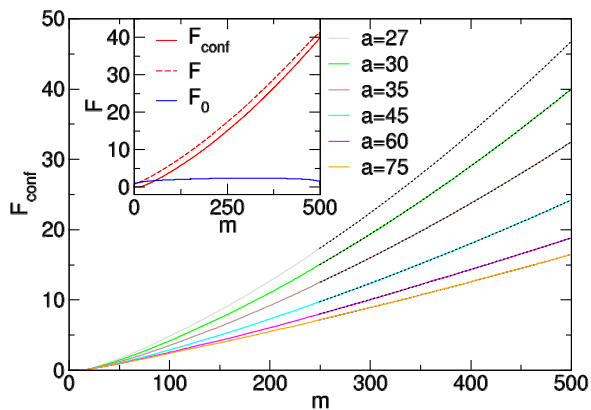


FIG. 9. Confinement free energy of a polymer chain of length $N = 500$ with bending rigidity $\kappa = 5$. The chain is confined to a rectangular cavity of dimensions $a \times a \times d$. Results are shown for $d = 20$ and various values of a . The inset illustrates the evaluation of F_{conf} as the difference between $F_1(m)$ and $F_0(m)$, as described in the text.

- ¹W. Reisner, J. N. Pedersen, and R. H. Austin, *Rep. Prog. Phys.* **75**, 106601 (2012).
- ²J. Z. Y. Chen, *Prog. Polym. Sci.* **54**, 3 (2016).
- ³L. Dai, C. B. Renner, and P. S. Doyle, *Adv. Colloid Interface Sci.* **232**, 80 (2016).
- ⁴K. Frykholm, V. Müller, K. Sriram, K. D. Dorfman, and F. Westerglund, *Q. Rev. Biophys.* **55**, e12 (2022).
- ⁵E. A. Strychalski, J. Geist, M. Gaitan, L. E. Locascio, and S. M. Stavis, *Macromolecules* **45**, 1602 (2012).
- ⁶P.-k. Lin, C.-C. Hsieh, Y.-L. Chen, and C.-F. Chou, *Macromolecules* **45**, 2920 (2012).
- ⁷K. D. Dorfman, D. Gupta, A. Jain, A. Muralidhar, and D. R. Tree, *Eur. Phys. J.: Spec. Top.* **223**, 3179 (2014).
- ⁸Y.-L. Chen, Y.-H. Lin, J.-F. Chang, and P.-k. Lin, *Macromolecules* **47**, 1199 (2014).
- ⁹D. R. Tree, W. F. Reinhart, and K. D. Dorfman, *Macromolecules* **47**, 3672 (2014).
- ¹⁰J. S. Leith, A. Kamanzi, D. Sean, D. Berard, A. C. Guthrie, C. M. McFaul, G. W. Slater, H. W. de Haan, and S. R. Leslie, *Macromolecules* **49**, 9266 (2016).
- ¹¹G. K. Cheong, X. Li, and K. D. Dorfman, *Phys. Rev. E* **97**, 022502 (2018).
- ¹²Y. Teng, N. T. Andersen, and J. Z. Y. Chen, *Macromolecules* **54**, 8008 (2021).
- ¹³M. P. Taylor, *J. Chem. Phys.* **157** (2022).
- ¹⁴D. Nykypanchuk, H. H. Strey, and D. A. Hoagland, *Science* **297**, 987 (2002).
- ¹⁵D. Nykypanchuk, H. H. Strey, and D. A. Hoagland, *Macromolecules* **38**, 145 (2005).

- ¹⁶J.-W. Yeh, A. Taloni, Y.-L. Chen, and C.-F. Chou, *Nano letters* **12**, 1597 (2012).
- ¹⁷K. L. Kounovsky-Shafer, J. P. Hernández-Ortiz, K. Jo, J. J. Odijk, Theo sand De Pablo, and D. C. Schwartz, *Macromolecules* **46**, 8356 (2013).
- ¹⁸R. Marie, J. N. Pedersen, D. L. Bauer, K. H. Rasmussen, M. Yusuf, E. Volpi, H. Flyvbjerg, A. Kristensen, and K. U. Mir, *Proc. Natl. Acad. Sci. USA* **110**, 4893 (2013).
- ¹⁹S. Lameh, T. Zhao, and D. Stein, *Phys. Rev. Appl.* **16**, 024019 (2021).
- ²⁰Y. Zhang, X. Liu, Y. Zhao, J.-K. Yu, W. Reisner, and W. B. Dunbar, *Small* **14**, 1801890 (2018).
- ²¹X. Liu, P. Zimny, Y. Zhang, A. Rana, R. Nagel, W. Reisner, and W. B. Dunbar, *Small* **16**, 1905379 (2020).
- ²²A. Rand, P. Zimny, R. Nagel, C. Telang, J. Mollison, A. Bruns, E. Leff, W. W. Reisner, and W. B. Dunbar, *ACS nano* **16**, 5258 (2022).
- ²³M. B. Mikkelsen, W. Reisner, H. Flyvbjerg, and A. Kristensen, *Nano Lett.* **11**, 1598 (2011).
- ²⁴C. L. Vestergaard, M. B. Mikkelsen, W. Reisner, A. Kristensen, and H. Flyvbjerg, *Nat. Commun.* **7**, 10227 (2016).
- ²⁵C. L. Smith, A. H. Thilsted, J. N. Pedersen, T. H. Youngman, J. C. Dyrnum, N. A. Michaelsen, R. Marie, and A. Kristensen, *ACS Nano* **11**, 4553 (2017).
- ²⁶J. Del Bonis-O'Donnell, W. Reisner, and D. Stein, *New J. Phys.* **11**, 075032 (2009).
- ²⁷A. R. Klotz, H. B. Brandao, and W. W. Reisner, *Macromolecules* **45**, 2122 (2012).
- ²⁸A. R. Klotz, M. Mamaev, L. Duong, H. W. de Haan, and W. W. Reisner, *Macromolecules* **48**, 4742 (2015).
- ²⁹A. R. Klotz, L. Duong, M. Mamaev, H. W. de Haan, J. Z. Y. Chen, and W. W. Reisner, *Macromolecules* **48**, 5028 (2015).
- ³⁰A. R. Klotz, H. W. de Haan, and W. W. Reisner, *Phys. Rev. E* **94**, 042603 (2016).
- ³¹D. Kim, C. Bowman, J. T. Del Bonis-O'Donnell, A. Matzavinos, and D. Stein, *Phys. Rev. Lett.* **118**, 048002 (2017).
- ³²S. Kumar, J. M. Rosenberg, D. Bouzida, R. H. Swendsen, and P. A. Kollman, *J. Comput. Chem.* **16**, 1339 (1995).
- ³³C. Micheletti, D. Marenduzzo, and E. Orlandini, *Phys. Rep.* **504**, 1 (2011).
- ³⁴D. Frenkel and B. Smit, *Understanding Molecular Simulation: From Algorithms to Applications*, 2nd ed. (Academic Press, London, 2002).
- ³⁵M. P. Allen and D. J. Tildesley, *Computer Simulation of Liquids*, 2nd ed. (Oxford University Press, Oxford, 2017).
- ³⁶M. Doi and S. F. Edwards, *The Theory of Polymer Dynamics*, International Series of Monographs on Physics, Vol. 73 (Oxford University Press, Oxford, 1986).
- ³⁷T. W. Burkhardt, *J. Phys. A: Math. Gen.* **30**, L167 (1997).
- ³⁸J. Z. Y. Chen and D. E. Sullivan, *Macromolecules* **39**, 7769 (2006).
- ³⁹H. W. de Haan and T. N. Shendruk, *ACS Macro Letters* **4**, 632 (2015).
- ⁴⁰J. M. Polson and D. R. Heckbert, *Phys. Rev. E* **100**, 012504 (2019).
- ⁴¹B. Kundukad, J. Yan, and P. S. Doyle, *Soft matter* **10**, 9721 (2014).
- ⁴²G. S. Grest and K. Kremer, *Phy. Rev. A* **33**, 3628 (1986).
- ⁴³J. M. Polson and Z. R. N. McLure, *Phys. Rev. E* **99**, 062503 (2019).